Discharge phenomena of an atmospheric pressure radio-frequency capacitive plasma source

Jaeyoung Park,[a] I. Henins, H. W. Herrmann, and G. S. Selwyn
Plasma Physics Division, Los Alamos National Laboratory, Los Alamos, New Mexico 87545

R. F. Hicks
Chemical Engineering Department, University of California, Los Angeles, California 90095

(Received 3 July 2000; accepted for publication 13 September 2000)

Discharge phenomena of a nonthermal atmospheric pressure plasma source have been studied. An atmospheric pressure plasma jet (APPJ) operates using rf power and produces a stable homogeneous discharge at atmospheric pressure. After breakdown, the APPJ operation is divided into two regimes, a ''normal'' operating mode when the discharge is stable and homogeneous, and a ''failure'' mode when the discharge converts into a filamentary arc. Current and voltage ($I-V$) characteristics and spatially resolved emission intensity profiles have been measured during the normal operating mode. These measurements show that the APPJ produces an alpha (α) mode rf capacitive discharge. Based upon a dimensional analysis using the observed $I-V$ characteristics, a rough estimate is made for plasma density of $3\times10^{11}\ \mathrm{cm}^{-3}$ and an electron temperature of 2 eV. In addition, the gas temperature of 120 °C has been spectroscopically measured inside the discharge. These plasma parameters indicate that the APPJ shows promise for various materials applications as it can produce substantial amounts of reactive species and avoid thermal damages, while having the advantage of atmospheric pressure operation. © 2001 American Institute of Physics.
[DOI: 10.1063/1.1323753]

I. INTRODUCTION

Plasma processing of materials is a vital industrial technology in many areas including electronics, aerospace, automotive, and biomedical industries. This is because of the unparalleled capability of plasmas for production of chemically reactive species at a low gas temperature while maintaining high uniform reaction rates over relatively large areas.[1,2] Currently, the majority of plasma processing is done at low pressure and the vacuum operation is viewed as a necessary requirement. In principle, however, atmospheric pressure plasmas can provide a critical advantage over widely used low pressure plasmas [e.g., magnetron, reactive ion etchers (RIEs), inductively coupled plasmas (ICP), etc.], as they do not require expensive and complicated vacuum systems. Without a vacuum system, the cost of materials processing could be reduced substantially and materials issues related to vacuum compatibility would not be of concern. Therefore, the use of atmospheric pressure plasmas could greatly expand the current scope of materials processing.[3]

Recently, a few novel atmospheric pressure discharge sources have been developed. These sources show promise to potentially replace low pressure plasmas devices for some existing applications and to create new applications. These sources include the atmospheric pressure plasma jet (APPJ),[3–7] the cold plasma torch,[8] the one atmosphere uniform glow discharge plasma (OAUGDP),[9] the microhollow cathode discharge,[10] and the surface-wave discharge.[11] Though different in dimensions, electrode materials, and frequencies of the electric fields (dc to a few GHz), these sources share some common aspects. They produce discharges with a low gas temperature, typically below 300 °C (with exceptions of the microhollow cathode discharge and the surface-wave discharge), and provide reasonable reaction rates for etching, ashing, and deposition over limited areas. Furthermore, it is indicated that these sources may produce discharges that resemble low pressure glow discharges and share some of the merits of the low pressure plasma sources. These observations prompt a detailed study in characterizing and understanding the discharge phenomena of these novel atmospheric pressure sources.

On the other hand, rf capacitive discharges at intermediate pressure (10–200 Torr) have been used extensively since the 1980's for high power gas lasers, such as CO_2 lasers.[12–15] Compared to dc excitation, the use of rf fields provided improved discharge stability and increased maximum laser outputs with higher overall efficiency. In general, rf capacitive discharges at intermediate pressure can exist in two distinctively different but stable modes, α and γ mode, depending on the dominant ionization mechanism.[15–18] In the α mode, the discharge is sustained by volumetric ionization processes, while ionization by secondary electrons from the electrode surfaces is important in the γ mode. Of these two modes, it is found that only the α-mode operation provides desired discharge conditions for laser excitation. This is because the electron impact excitation essential for population inversion occurs efficiently throughout the discharge volume in the α mode. In the γ mode, the input power is dissipated mostly in the small volume of sheaths near the electrodes

[a]Author to whom correspondence should be addressed; electronic mail: jypark@lanl.gov

 © 2001 American Institute of Physics

Downloaded 17 Jan 2003 to 128.97.84.125. Redistribution subject to AIP license or copyright, see http://ojps.aip.org/japo/japcr.jsp

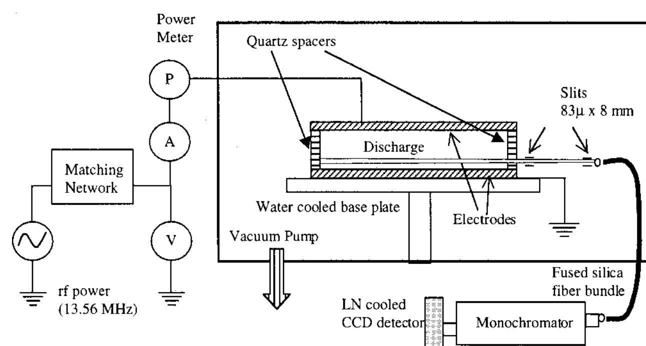

FIG. 1. Schematic of the experimental setup. For electrical measurements, the discharge system is placed in a vacuum chamber to reduce impurities in the discharge and to operate at the desired gas pressure, up to atmospheric pressure. In the case of optical emission measurements, the electrode assembly was replaced by a plasma source operating outside the vacuum chamber. This change is made to provide spatially resolved emission intensity profile between the electrodes.

without contributing much to the lasing efficiency. In addition, the gas temperature in the discharge tends to be higher for the γ mode compared to the α mode. Thus, it is of interest to investigate whether an α-mode rf capacitive discharge can be produced at atmospheric pressure and, if so, whether it can be used for materials applications.

In this article, we present and analyze experimental results of the APPJ operation. Emphasis will be given to the characterization of the discharge produced in APPJ and the evaluation of its potential for materials applications. The experimental setup is given in Sec. II. In Sec. III, we present the experimental results. Discussion of the experimental results is given in Sec. IV, conclusions follow in Sec. V.

II. EXPERIMENTAL SETUP

A schematic of the experimental setup is shown in Fig. 1. The discharge used for this study was produced between two planar square electrodes: a rf powered top electrode and a grounded, water cooled bottom electrode. Measurements were conducted for different electrode materials, such as aluminum, copper, molybdenum, and stainless steel, to investigate the effects of the electrode surface properties on the discharge. The surface area of each electrode was 100 cm^2 and the gap spacing between the electrodes was varied from 0.16 to 0.32 cm using two quartz spacers which also provided optical access to the discharge region. To minimize impurities in the discharge, the discharge assembly was placed in a vacuum chamber, pumped by a 500 1/s turbopump. The base pressure of the vacuum chamber was 3×10^{-7} Torr. During the experiments, the chamber was pumped out below 1×10^{-3} Torr and filled with a high purity gas (99.9995% or better for helium, argon, and oxygen, and 99.95% or better for nitrogen) mixture at room temperature and at pressures ranging from 300 to 600 Torr. The atmospheric pressure in Los Alamos is about 590 Torr due to the altitude, which limits the gas pressure below 600 Torr to avoid overpressure in the vacuum chamber. As reported previously, the APPJ has been operated successfully at sea level and no major difference is observed in the electrical characteristics.[4,5]

The electrical properties of the discharge were studied by simultaneously measuring the voltage across the discharge and the rf current. The measurements were made using a high voltage probe (Tektronix P6015A with a bandwidth of 75 MHz) and a current probe (Ion Physics current monitor CM-10-M with a bandwidth of 20 MHz). The results were recorded on a digital oscilloscope (Tektronix TDS 640 with sampling rate of a 2 G samples/s and a bandwidth of 500 MHz). The deviation from linear response of the current probe was less than 20% up to 35 MHz, as tested by using a 50 Ω dummy load. For measurements done at 13.56 MHz, a tuned impedance probe (Advanced Energy rfZ 60 probe) was also used to measure the amplitudes of the discharge voltage and the rf current along with the coupled power to the plasma. The agreement between the two measurements was reasonable (within 15%).

In addition, the light emission from the discharge was measured. As shown in Fig. 1, the collection optics for the emission measurement consists of a collimating slit assembly, a fiber bundle, and a monochromator with a liquid nitrogen cooled charge coupled device (CCD) array detector. For these measurements, the electrode assembly was replaced by a plasma source with the same electrode configuration including a water cooled ground electrode, operating outside the vacuum chamber. This is because of the difficulty of accurately locating and moving the slit assembly relative to the electrodes inside the vacuum chamber. This plasma source is identical to the one used in our previous study except for narrower electrodes (1.5 cm wide and 10 cm long).[7] The use of the narrower electrodes, coupled with the slit assembly (two 8 mm by 83 μm slits, separated by 2.5 cm), was to measure the emission intensity profile between the electrodes with a spatial resolution of 150 μm. To reduce the air contamination in the discharge, a gas mixture was flowed at a rate of 50 slpm. Still, some impurities like nitrogen and water vapor were detected from the emission spectrum due to the back diffusion of air and imperfect seal of the electrode assembly. However, these impurity concentrations were low and the electrical properties of the discharge showed no change compared with the measurements taken in the vacuum chamber. For a given gap spacing, the discharge voltage is nearly constant while the current and the input power vary linearly with the electrode area. Thus, the emission measurements were compared with other results as a function of input power per given electrode surface area. In addition, the gas temperature of the discharge was measured spectroscopically by fitting the rotational intensity distribution of the oxygen atmospheric band at 762 nm ($b^1\Sigma_g^+ \rightarrow X^3\Sigma_g^-$) to a Maxwell–Boltzmann distribution using a gas mixture of helium (99.6%) and oxygen (0.4%).

Unless specified otherwise, the baseline discharge conditions are as follows: pure helium feedgas, rf frequency of 13.56 MHz, gas pressure = 600 Torr, aluminum electrodes, electrode gap spacing = 0.16 cm, and electrode area = 100 cm^2. All voltages and currents are rms values unless specified otherwise.

Downloaded 17 Jan 2003 to 128.97.84.125. Redistribution subject to AIP license or copyright, see http://ojps.aip.org/japo/japcr.jsp

III. EXPERIMENTAL RESULTS

A. Visual description of the discharge

A discharge in the APPJ is initiated once the breakdown voltage is reached and light emission from the plasma is observed. Initially the plasma covers only a small area of the electrodes and often moves around. With increasing input power, it quickly spreads to cover the entire volume between the electrodes. Visually, the discharge appears uniform throughout the volume and has a white-purplish glow, without any sign of filamentation or arcing. The plasma is volumetric in space and homogeneous in time, as indicated by the measured optical emission intensity from the discharge.[7] A further increase in input power gradually raises the plasma emission intensity and causes a brighter emission near the electrodes than in the middle. When the input power is raised above a critical level, the discharge suddenly turns into a filamentary arc, causing a highly localized and bright orange emission. Based on the various operating conditions, such as gas pressure and gap spacing, the filamentary arc either coexists with a uniform glow or suppresses the plasma elsewhere. Usually, the arc is more intense and damaging when the filamentary arc suppresses the plasma elsewhere. Generally, one arc spot of a few millimeters in size is observed on each electrode. The arc spots either move around the electrodes or stay in one location. When the arc is left on for over 5–10 s, physical damage to the electrodes is usually observed, caused by the intense heating of the electrodes at the arc spots. The transition to an arc is irreversible as the arc spots remain even after the input power is reduced below the critical level of arcing. Only when the input power is sufficiently reduced, the arc spots disappear. When the arc had coexisted with a uniform glow, the discharge again becomes uniform in space. However, the arc spots persist until the discharge is extinguished when the filamentary arc suppressed the plasma elsewhere.

B. Voltage and current waveforms

Figure 2 shows waveforms of the discharge voltage (solid line) and the rf current (dotted line) for various input power levels in a pure helium discharge. At low power, both waveforms are smooth and nearly sinusoidal, indicating a mostly linear response of the discharge, as shown in Fig. 2(a) at 124 W. In addition, the capacitive nature of the discharge is clearly shown as the current waveform leads the voltage waveform by 63°. With increasing input power, both waveforms exhibit minor distortion, as shown in Fig. 2(b) at 357 W. The amplitude (not the rms value) of the discharge voltage increases less than linearly from 220 to 260 V with an increase in rf current from 2.2 to 5.4 A.

In comparison, Fig. 2(c) shows the voltage and the current waveforms when the discharge becomes an arc after the input power is raised above a critical level. Both the current and the voltage waveforms exhibit large distortion and the current waveform now trails the voltage waveform by 29°. This change in the phase relation is attributed to the resistive nature of the arc discharge and to a large inductance, caused by a high rf current density in the filamentary arc, exceeding the capacitance outside the arc spots. As mentioned earlier,

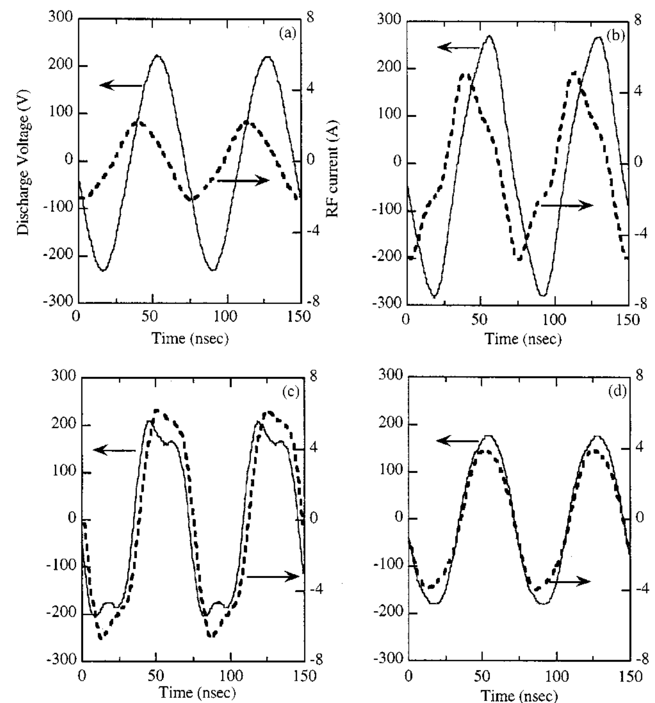

FIG. 2. Waveforms of the discharge voltage (solid line) and the rf current (dotted line) for various input powers in a pure helium discharge. Discharge parameters are: gap spacing=0.16 cm, electrode area=100 cm^2, gas pressure=600 Torr, and rf frequency=13.56 MHz. Initially, the input power was raised to (a) 124 W, to (b) 357 W, and to (c) 704 W before being reduced to (d) 372 W.

the arc persists even when the input power is reduced below the critical level of arcing. This is shown in Fig. 2(d) when the input power is reduced to 372 W after arcing. The voltage and current waveforms are nearly sinusoidal and in phase, very different from the waveforms at a similar input power in Fig. 2(b).

C. Current and voltage ($I-V$) characteristics

Different operating regimes of the APPJ can be identified and characterized using the relation between the amplitudes of the rf current and the discharge voltage. In this article, the term "$I-V$ curve" is used for this relation, while the term "$I-P$ curve" is used for the relation between the amplitudes of the rf current and the input power. In Fig. 3, a $I-V$ curve and an $I-P$ curve are shown for a pure helium discharge at 600 Torr. Prior to breakdown, the load is purely capacitive and both the rf current and the discharge voltage increase linearly with a 90° phase difference between them. Once the applied voltage reaches the breakdown voltage, the discharge is initiated and operates at a lower voltage compared to the breakdown voltage. This is shown as a discontinuity in the $I-V$ curve.

With increasing input power, both the rf current and the discharge voltage increase monotonically until the discharge turns into an arc. It is noted that the slope of the $I-V$ curve in this region is less than linear. This region of the $I-V$ curve represents the normal operating mode of the APPJ, as the discharge is stable and uniform. The waveforms in Figs. 2(a) and 2(b) were obtained in this region of the $I-V$ curve.

Downloaded 17 Jan 2003 to 128.97.84.125. Redistribution subject to AIP license or copyright, see http://ojps.aip.org/japo/japcr.jsp

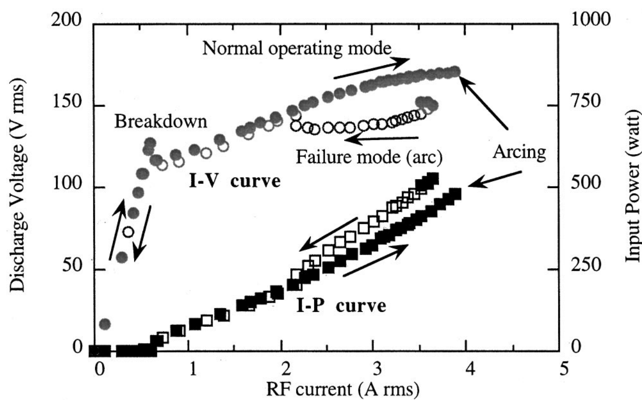

FIG. 3. Amplitudes of discharge voltage ($I-V$ curve) and input power ($I-P$ curve) as a function of rf current. The discharge parameters are the same as in Fig. 2. Operating regimes are divided between the normal operating mode and the failure mode. Closed symbols are data points with increasing input power and open symbols are data points with decreasing input power.

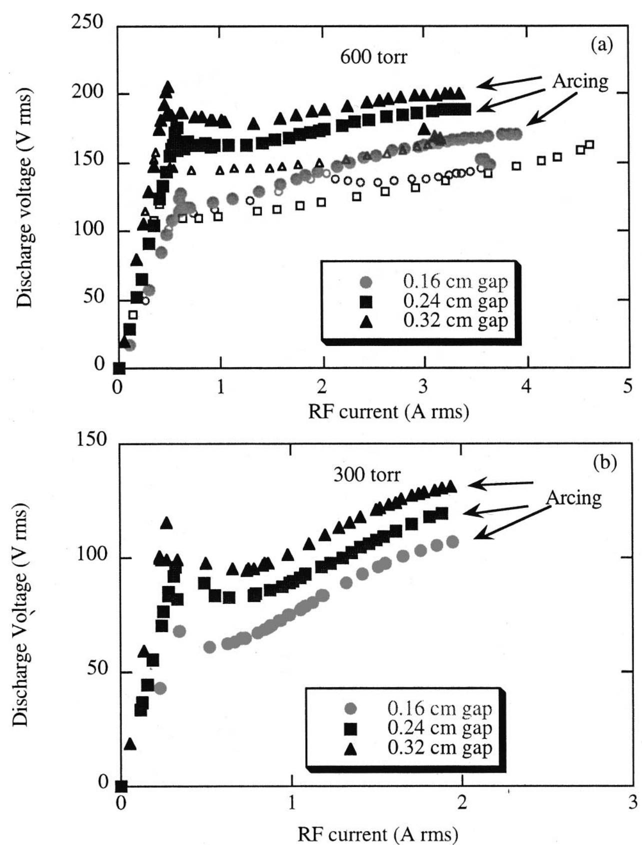

FIG. 4. $I-V$ curves as a function of gap spacing in pure helium discharges for two different gas pressures: 600 Torr for (a) and 300 Torr for (b). A rf frequency of 13.56 MHz was used with an electrode area of 100 cm^2. In (a), closed symbols are the data points with increasing input power and open symbols are data points with decreasing input power; (b) only the data points prior to arcing are shown to clarify the behavior of $I-V$ in the normal operating regime. Note that different scales are used for (a) and (b).

It is noted that little difference is observed in the $I-V$ curves for different electrode materials in the normal operating regime.

As mentioned earlier, the discharge turns into an arc, when the input power is raised above a critical level. The transition to an arc is represented by discontinuities in the $I-V$ and $I-P$ curves. Again, little difference is observed in the critical input power level among different electrode materials (aluminum, copper, molybdenum, and stainless steel). However, it should be noted that the present study does not cover the $I-V$ curve after arcing in detail, because prolonged arcing often causes the damage to electrodes. The irreversible nature of the transition to an arc is clearly shown by the $I-V$ and $I-P$ curves. After arcing, these curves occupy different paths, characterized by a lower discharge voltage and a higher input power for a given rf current. This region of the $I-V$ curve represents the failure mode of the APPJ. The waveforms in Figs. 2(c) and 2(d) were obtained from this region of the $I-V$ curve. With decreasing input power, the $I-V$ curve merges with the path prior to arcing, as shown in Fig. 3, if the arc coexists with a uniform glow. However, the $I-V$ curve does not merge with the path prior to arcing, if the arc suppresses the plasma elsewhere, as shown in Fig. 4(a). In general, the arc tends to suppress the discharge elsewhere when the gap spacing or the gas pressure is increased. It is noted that a slightly lower discharge voltage is usually observed for a given rf current after the $I-V$ curve merges back to the path prior to arcing due to the heating of the gas by the plasmas.

In Fig. 4, $I-V$ curves are shown as a function of electrode gap spacing for two different gas pressures, 300 and 600 Torr. Different slopes in the $I-V$ curve prior to breakdown reflect the difference in the vacuum capacitance. In the normal operating mode, the discharge voltage is higher for wider gap spacing at a given rf current. It is noted that the voltage difference between two different gap spacings is nearly constant for different rf currents except for the region near breakdown. For the same pair of gap spacings, the voltage difference is lower at 300 Torr than at 600 Torr. At 600 Torr, the voltage difference is 23–30 V between the gap spacings of 0.16 and 0.24 cm, and about 15 V between the gap spacings of 0.24 and 0.32 cm. At 300 Torr, the voltage difference is 12–13 V for both pairs of gap spacings. In addition, arcing occurs at about the same rf current within 15% regardless of the gap spacing for a given gas pressure. Once the discharge turns to an arc, the $I-V$ curve follows one of the two distinctive paths, as discussed earlier. For example, the $I-V$ curve merges with the path prior to arcing for the 0.16 cm gap spacing, while it departs from the path prior to arcing for the 0.24 and 0.32 cm gap spacings in Fig. 4(a). Henceforth, only the data points prior to arcing will be shown to clarity the $I-V$ curve during the normal operating mode.

In Fig. 5, $I-V$ curves are shown for different gas pressures at a gap spacing of 0.24 cm. In the normal operating mode, the discharge voltage is higher for higher gas pressure at a given rf current. Unlike Fig. 4, arcing occurs at a higher rf current and at a higher input power for a higher gas pressure.

In Fig. 6, $I-V$ curves are shown for different rf frequencies. The discharge voltage decreases with increasing rf frequency for a given rf current, as does the slope of the $I-V$ curve. In addition, the discharge is more stable with increasing rf frequency as indicated by the extended $I-V$ curves to

Downloaded 17 Jan 2003 to 128.97.84.125. Redistribution subject to AIP license or copyright, see http://ojps.aip.org/japo/japcr.jsp

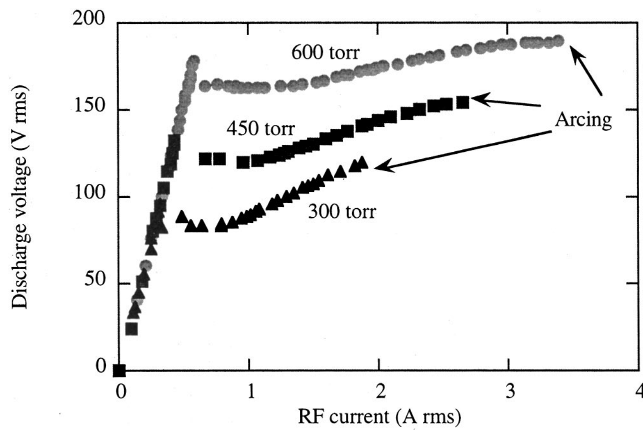

FIG. 5. $I-V$ curves as a function of gas pressure in a pure helium discharge. Discharge parameters are: gap spacing=0.24 cm, electrode area=100 cm^2, and rf frequency=13.56 MHz. Only the data points prior to arcing are shown.

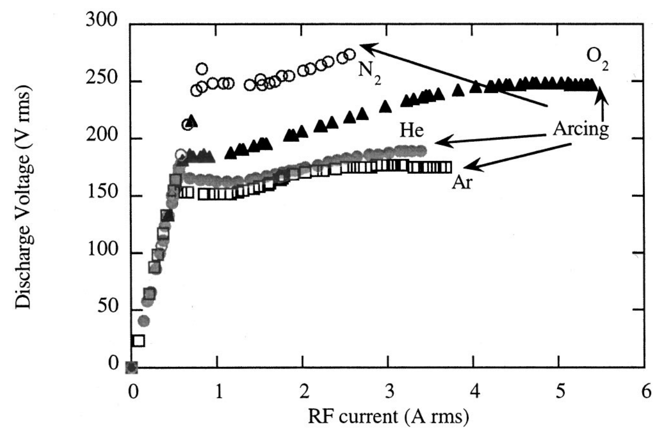

FIG. 7. $I-V$ curves as a function of gas composition for pure helium and for 1% addition of argon, nitrogen, and oxygen to pure helium. Discharge parameters are: gap spacing=0.24 cm, gas pressure=600 Torr, electrode area=100 cm^2, and rf frequency=13.56 MHz. Only the data points prior to arcing are shown. Though not shown in the figure, the critical input powers above which discharge turns to an arc are: 510 W for pure helium, 550 W for 1% argon, 1070 W for 1% oxygen, and 490 W for 1% nitrogen.

higher rf currents. For 10 MHz, the discharge turns into an arc at about 300 W but this occurs at 430 W for 13.56 MHz. For 20 MHz, we were not able to initiate an arc because the maximum power was limited by the output capacity of our variable frequency rf power supply rated at 500 W.

In Fig. 7, $I-V$ curves are shown for different gas mixtures with a gap spacing of 0.24 cm. The $I-V$ curves show substantial changes when a relatively small fraction (1%) of another gas is added to the helium. The discharge voltage is much higher for a given current when 1% of oxygen or nitrogen is added, compared to a pure helium discharge. On the other hand, the discharge voltage decreases slightly for a given rf current for addition of argon. In addition, substantial differences in the onset of arcing are observed among the different gas mixtures. In terms of input power, the critical input power for arcing varies from 510 W for pure helium to 550 W for 1% addition of argon, to 1070 W for 1% addition of oxygen, and to 490 W for 1% addition of nitrogen.

D. Emission intensity profile between the electrodes

Figure 8 shows spatial profiles of emission intensity between the electrodes for a pure helium discharge at 600 Torr. The input powers were 25 and 50 W for an electrode area of 15 cm^2 (1.5 cm wide and 10 cm long) and a gap spacing of 0.16 cm. These are equivalent to 167 and 333 W of input powers for the 100 cm^2 electrodes that are used for all other measurements in this study. The corresponding discharge voltages are 140 and 163 V, respectively, while the current densities are 0.018 and 0.03 A/cm^2. The emission intensity profile is nearly symmetrical though small asymmetry is seen due to the watercooling of the ground electrode. The emission intensity is low both near the electrodes and in the middle of the discharge, and rises to the maximum at some distance away from the electrodes. This intensity profile is an important characteristic of the normal operating regime of the APPJ, as the shape of the profile stays invariant for dif-

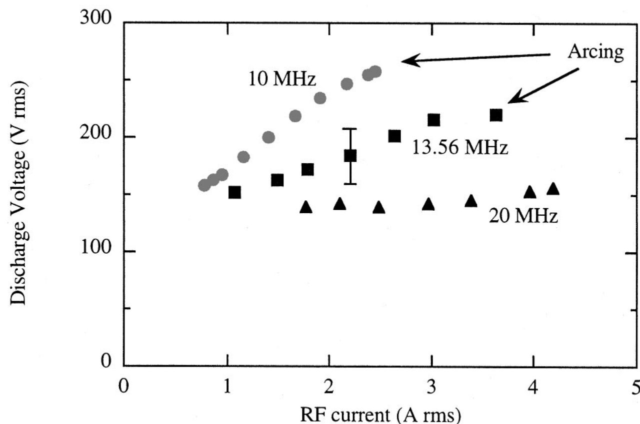

FIG. 6. $I-V$ curves as a function of rf frequency in a pure helium discharge. Discharge parameters are: gap spacing=0.16 cm, electrode area=100 cm^2, and gas pressure=600 Torr. Note that the arcing was not observed for 20 MHz due to the output capacity limit of the variable frequency rf power supply rated at 500 W.

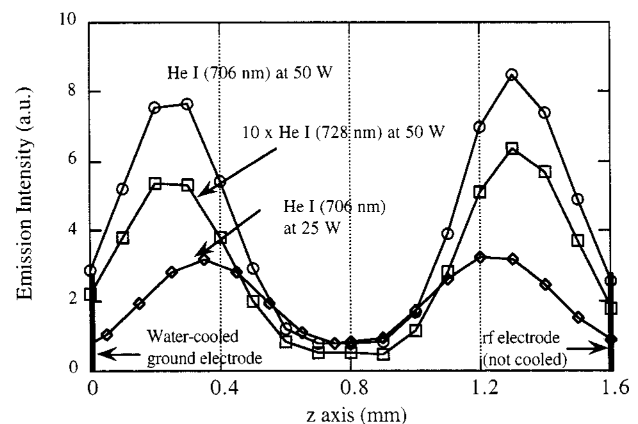

FIG. 8. Spatial profiles of emission intensity between the electrodes for a pure helium discharge for two input powers (25 and 50 W). Discharge parameters are: gap spacing=0.16 cm, gas pressure=600 Torr, rf frequency=13.56 MHz, and electrode area=15 cm^2.

Downloaded 17 Jan 2003 to 128.97.84.125. Redistribution subject to AIP license or copyright, see http://ojps.aip.org/japo/japcr.jsp

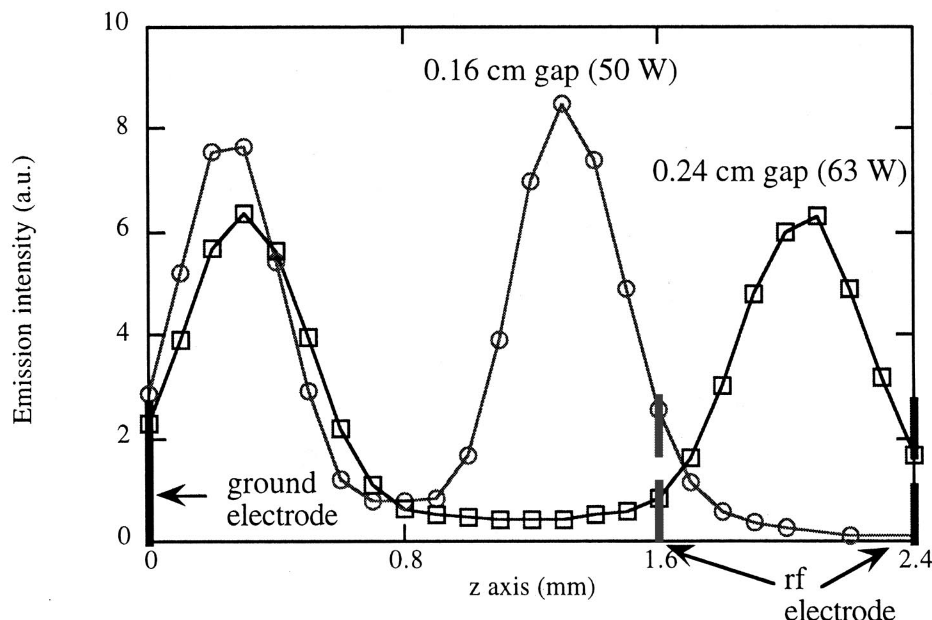

FIG. 9. Emission intensity profiles for different gap spacings of 0.16 and 0.24 cm, at the same rf current density of 0.03 A/cm^2. Discharge parameters are: gas pressure=600 Torr, rf frequency =13.56 MHz, electrode area=15 cm^2, and input powers=50 and 63 W.

ferent input power, gap spacing, rf frequency, and gas mixture. The location of the maximum intensity is about 0.35 mm away from the electrode at 25 W and moves closer to the electrode with increasing input power, about 0.28 mm away from the electrode at 50 W. As shown in Fig. 8, the location of the maximum intensity varies little for different helium emission lines.

When the gap spacing is increased to 0.24 cm, the location of the emission intensity maximum changes little for a constant discharge current density (0.03 A/cm^2), as shown in Fig. 9. The discharge voltage was 187 V and the input power was 63 W, corresponding to 420 W of input power for the 100 cm^2 electrodes.

E. Gas temperature measurement

In Fig. 10, an emission spectrum of the oxygen atmospheric band at 762 nm is shown with a Maxwell–Boltzmann rotational intensity distribution at 120 °C.[19–21] The input power was 400 W using the 100 cm^2 electrodes. The uncertainty of the fit is ±25 °C. The spectrum was taken from the middle of a discharge using a gas mixture of helium (99.6%) and oxygen (0.4%) at a flow rate of 50 slpm. The spectral resolution of the optical system is about 0.02 nm using a 0.64 m monocromator with a grating of 2400 groove/mm. Because of very frequent collisions at atmospheric pressure, the gas temperature of the discharge should be equal to

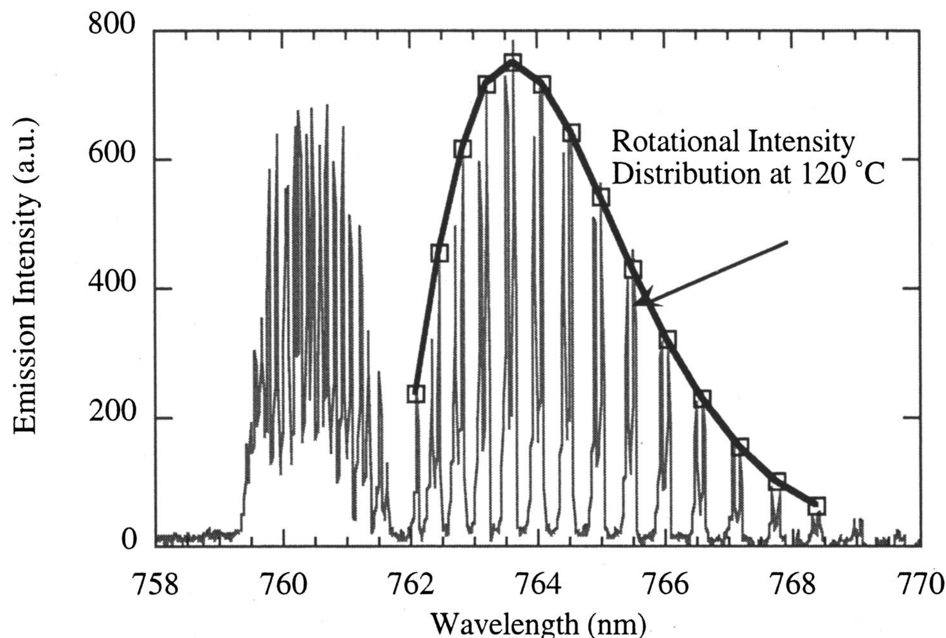

FIG. 10. Emission spectrum of the oxygen atmospheric band at 762 nm with a calculated rotational intensity distribution at 120 °C. Discharge parameters are: gap spacing=0.16 cm, gas pressure=600 Torr, rf frequency=13.56 MHz, electrode area =100 cm^2, input power=400 W, and gas composition=99.4% helium and 0.4% oxygen. Note a doublet-like structure of the emission spectrum in the long wavelength region. This is because the oxygen atmospheric band is both a magnetic dipole transition and an intercombination transition, and the band has four branches, ^RR, ^RQ, ^PQ, and ^PP based on two sets of selection rules (see Refs. 19 and 21).

Downloaded 17 Jan 2003 to 128.97.84.125. Redistribution subject to AIP license or copyright, see http://ojps.aip.org/japo/japcr.jsp

the rotational temperature of the $O_2(b^1\Sigma_g^+)$ molecules. This measured gas temperature of 120 °C is consistent with a thermocouple measurement of 90 °C outside the discharge region.

IV. DISCUSSION

A key finding of the present study is that the discharge produced in the APPJ is essentially an α-mode capacitive discharge at atmospheric pressure. This finding is based on the following comparison between the experiments and the previous studies on rf α-mode capacitive discharges, in particular the works by Vidaud, Durrani, and Hall,[18] and by Raizer, Shneider, and Yatsenko.[15] The current and voltage waveform measurements in Figs. 2(a) and 2(b) show that the APPJ discharge operating in the normal mode is clearly capacitive and different from arc-type discharges. In addition, the observed $I-V$ characteristics of the APPJ and its functional dependence on the gas pressure and rf frequency is very similar to those of α-mode discharges for gas lasers. It is further noted that the observed $I-V$ characteristics in the normal operating regime vary little with electrode materials, thus indicating the passive role of the electrodes in the discharge associated with the α-mode discharge. In comparison, the electrode surface property plays a significant role in determining the discharge characteristics in the γ mode because of the importance of secondary electrons in the ionization processes. Finally, the spatially resolved emission intensity profiles in Figs. 8 and 9 clearly show that the APPJ produces the α-mode discharge not the γ mode in the normal operating regime.

However, it is noted that we do not have a clear understanding of the nature of the failure mode in the APPJ at this point. This is because the discharge in the failure mode resembles a filamentary arc rather than a γ mode. As described in Sec. III B, the discharge becomes highly localized visually and severe thermal damage to the electrode is likely once the transition is made from the α mode above the critical input power. In addition, the current and voltage waveform measurements in Figs. 2(c) and 2(d) indicate that the discharge in the failure mode is mostly resistive rather than capacitive as expected for a γ-mode discharge. One possible explanation for the absence of the γ mode is that the γ mode may be unstable under the operating conditions used for the APPJ. Thus, the observed α mode to an arc transition may be the result of $\alpha-\gamma$ transition followed by arc formation due to the unstable nature of the γ-mode discharge in the APPJ. Though a more thorough investigation is needed to examine the exact nature of the failure mode in the APPJ, we will limit our discussion to the discharge physics during the α mode and the onset of the α-mode failure. This is because the practical applications using the APPJ source would be based mainly on the α-mode operation.

One of the essential features of the α-mode discharge is the space charge sheath near the electrodes. Here the discharge current is carried mostly by displacement current due to the depletion of electrons. Averaged over a rf period, the sheath possesses more ions than electrons, thus creating electric fields within it that accelerate the ions to the electrode and repels the electrons to maintain charge balance in the discharge. Outside the sheath, charge neutrality is closely attained and the bulk of the discharge current is carried by the electron conduction current. This spatial variation of electron density and electric fields explains the observed emission intensity profile in Figs. 8 and 9, since the electron impact excitation depends on both electron density and electron energy. The plasma emission is low close to the electrodes due to the depletion of electrons, while it is also low in the middle of the discharge as the electrons gain less energy from the lower electric fields. The plasma emission intensity reaches maximum as the effect from the high electron energy due to the strong electric fields outweighs the decrease in electron density. Typically, the maximum emission intensity occurs in the boundary region between the sheath and the bulk plasma. Thus, the emission intensity measurements in Figs. 8 and 9 indicate that the sheath thickness in the APPJ discharge is 0.28–0.35 mm.

In a simple dimensional model of the sheath, the relation among the discharge current, sheath voltage, and sheath thickness can be written in

$$I_{rf}=(i\omega C_{sheath})V_{sheath} \quad \text{and} \quad C_{sheath}=k\frac{\varepsilon A}{d_{sheath}}, \tag{1}$$

where I_{rf} is the rf discharge current, ω is the angular frequency of the rf fields, C_{sheath} is the sheath capacitance, V_{sheath} is the voltage across the sheath, k is a numerical constant on the order of unity describing a dielectric constant of the sheath, ε is the permittivity of the gas medium, A is the electrode area, and d_{sheath} is the sheath thickness. This simple sheath scaling can describe the electrical response of the sheath with an appropriate constant for the sheath dielectric constant. For example, the self-consistent rf capacitive sheath model by Liberman and Lichtenberg can be reduced to Eq. (1) with numerical constants of 1.23 for collisionless sheath (low pressure) and of 1.52 for collisional sheath (high pressure).[2,22] Using 1.52 for the collisional sheath in Eq. (1), the voltage across the sheath can be estimated from the observed sheath thickness and the rf current. From Fig. 8, the sheath thickness is about 0.35 mm for a rf current density of 0.018 A/cm^2, thus yielding a voltage across the sheath of 55 V. For a rf current density of 0.03 A/cm^2, the sheath thickness is about 0.28 mm, yielding a sheath voltage of 73 V. Since the discharge employs two symmetric electrodes, the sheath voltages of 55 and 73 V indicate that the majority of discharge voltage occurs in the sheath region, compared with the discharge voltages of 140 and 163 V. This large voltage drop in the sheath is an important property of rf capacitive discharges for both low and high gas pressures.[2,15,23] In addition, the less than linear slope in the $I-V$ curves in the normal operating mode may be related to the decrease in sheath thickness with input power according to Eq. (1).

Furthermore, Eq. (1) describes the observed decrease in discharge voltage and in the slope of $I-V$ curve with increasing rf frequency in Fig. 6. For a given sheath thickness, the required voltage across the sheath to drive the same amount of displacement current will decrease with increasing rf frequency. Since the sheath voltage is a large fraction of the discharge voltage, this explains a lower discharge voltage

Downloaded 17 Jan 2003 to 128.97.84.125. Redistribution subject to AIP license or copyright, see http://ojps.aip.org/japo/japcr.jsp

for a given rf current and a smaller slope of $I-V$ curve with increasing rf frequency. Similar results have been obtained in intermediate pressure rf α-mode discharges for gas lasers.[15,18] Furthermore, enhanced stability of the discharge at higher rf frequencies can be attributed to this smaller sheath voltage. For example, many high power gas lasers use rf frequency of 100 MHz or higher to increase discharge stability. However, it should be noted that increasing rf frequency does not guarantee increasing reactive species production, as in the case of gas lasers.[13] Also, the cost of the power supply, as well as the complexity of the plasma source, increases with increasing rf frequency. Thus, the choice of rf frequency for the optimum source operation requires consideration of discharge stability, efficiency, and cost for its use in materials applications.

Though there are substantial electric fields in the sheath, the dynamics of the charged particles in the sheath is markedly different at atmospheric pressure than at low pressure. In particular, ion acceleration in the sheath is very small at atmospheric pressure due to frequent collisions with neutrals. For example, if the sheath voltage of 73 V is distributed uniformly within 0.28 mm, the drift velocity of the ions would be $3.6\times10^4\ \mathrm{cm\,s^{-1}}$ at atmospheric pressure for a helium ion mobility of about 14 $\mathrm{cm^2/(V\,s)}$.[24–27] This corresponds to an ion energy gain of only 0.0027 eV in the sheath. Thus, plasma reaction with materials is driven mostly by neutral radicals and ion bombardment of plasma facing components is not significant for atmospheric pressure plasmas. As a result, damage to treated materials by energetic ions will be a nonissue at atmospheric pressure, and high etch selectivity can be obtained for plasma etching as the surface reaction is mostly chemically driven. However, the low directed ion energy in the sheath is not compatible with some applications, such as directional etching and ion-assisted chemical vapor deposition.

Another difference of atmospheric pressure plasmas, as compared to low pressure plasmas, is the presence of finite and relatively large electric fields in the bulk region to drive the electron conduction current because of the low mobility of electrons, as shown in

$$J_{\mathrm{rf}}\approx J_{\mathrm{cond}}^{e}=-n_e e\mu_e E_{\mathrm{bulk}}, \tag{2}$$

where J_{rf} and J_{cond}^{e} are the rf current density and the electron conduction current density in the bulk, μ_e is the electron mobility, and E_{bulk} is the electric field in the bulk region. It is assumed that the displacement current is small compared to the electron conduction current in the bulk region. This finite electric field can explain the observed increase in discharge voltage with increasing gap spacing in Fig. 4. As shown in Eq. (1), the voltage across the sheath depends on the discharge current and the sheath thickness. Since the sheath thickness changes little with gap spacing for a given rf current, as shown in Fig. 8, we can assume that the voltage across the sheath is approximately constant for different gap spacings. On the other hand, the voltage drop across the bulk region should increase for a larger gap due to the finite electric field in the bulk region, as shown in

$$\Delta V_{\mathrm{bulk}}=E_{\mathrm{bulk}}\Delta d_{\mathrm{bulk}}\approx\frac{J_{\mathrm{rf}}}{n_e e\mu_e}\Delta d_{\mathrm{bulk}}, \tag{3}$$

where ΔV_{bulk} is the voltage increase across the bulk region due to the change in thickness of the bulk region, and Δd_{bulk} is the change in thickness of the bulk region. In Fig. 4, the discharge voltage increase from 163 V at 0.16 cm to 187 V at 0.24 cm for a rf current density of 0.03 $\mathrm{A/cm^2}$. From Eq. (3), this corresponds to a bulk electric field of 300 V/cm, finite, but an order of magnitude smaller than the electric field in the sheath. The resulting displacement current density would be $2.3\times10^{-3}\ \mathrm{A/cm^2}$ for this time varying electric field of 300 V/cm, thus validating the assumption of small displacement in the bulk region. Equation (3) also explains the smaller increases in discharge voltage with increasing gap spacing at lower gas pressures. The electron mobility increases with decreasing gas pressure and a higher electron mobility would result in a lower voltage difference.

Furthermore, the electron density in the bulk can be estimated from Eq. (3). To conduct the rf current density of 0.03 $\mathrm{A/cm^2}$ under the electric field of 300 V/cm, the electron density needs to be $3.0\times10^{11}\ \mathrm{cm^{-3}}$ for an electron mobility of $2.1\times10^3\ \mathrm{cm^2/(V\,s)}$.[24–27] This electron density agrees reasonably well with a zero-dimensional power balance between electron heating by the rf fields and electron energy loss by collisions with neutrals, as shown in

$$P_{\mathrm{in}}\sim P_{\mathrm{loss}}\approx n_e\left(\frac{3}{2}kT_e-\frac{3}{2}kT_n\right)2\,\frac{m_e}{m_{\mathrm{He}}}\,\nu_{\mathrm{en}}\ \text{ in }\ \mathrm{W/cm^3}, \tag{4}$$

where P_{in} is the input power density, T_e is the electron temperature, T_n is gas temperature, m_e/m_{He} is the mass ratio between the electron and helium atom, and ν_{en} is the collision frequency of elastic scattering for electrons with helium atoms. For the electron temperature estimate, we will assume that the discharge voltage is uniformly distributed over the entire discharge volume by ignoring the difference in electric field strength between the sheath and the bulk region. This simplification is consistent with the zero-dimensional nature of the Eq. (4), where we are only interested in the average values over the entire discharge volume. Thus, the average electron characteristic energy would be 2.1 eV for the discharge voltage of 163 V over the 0.16 cm gap.[23–26] To estimate the gas temperature at 333 W, we will use the gas temperature measurement at 400 W in Fig. 10 and linearly interpolate its value:

$$T_n(333\,\mathrm{W})=T_n(\mathrm{room})+\tfrac{333}{400}[T_n(400\,\mathrm{W})-T_n(\mathrm{room})]. \tag{5}$$

From Eq. (5), the estimated gas temperature is 103 °C for a room temperature of 20 °C, yielding a gas density of $1.5\times10^{19}\ \mathrm{cm^{-3}}$. Using these values, we can calculate an electron density of $2.9\times10^{11}\ \mathrm{cm^{-3}}$ for an input power density of 20.8 $\mathrm{W/cm^3}$, consistent with the estimate using the electron conductivity.

The calculated electron density and characteristic electron energy indicate that the atmospheric pressure α-mode rf capacitive discharge produced in the APPJ shows promise for materials applications. The average electron energy of 2 eV is sufficient to produce reactive radicals, such as oxygen

Downloaded 17 Jan 2003 to 128.97.84.125. Redistribution subject to AIP license or copyright, see http://ojps.aip.org/japo/japcr.jsp

and fluorine atoms. This, coupled with the electron density on the order of $10^{11}\,\mathrm{cm}^{-3}$, explains the observed high production rate of reactive species in the APPJ, e.g., $[\mathrm{O}] \geq 5 \times 10^{15}\,\mathrm{cm}^{-3}$ when 1% of oxygen is added to the discharge.[7] This high concentration of reactive species in the discharge is in part due to the advantage of atmospheric pressure operation, compared to low pressure operation. Furthermore, the APPJ has been shown to etch polyimide, tungsten, tantalum, and silicon dioxide and to deposit silicon dioxide films at rates comparable to those achieved in low pressure discharge systems.[4,5] On the other hand, this moderate electron density separates the APPJ from existing high temperature atmospheric plasma sources such as plasma torches and arc discharges where the electron density generally exceeds $10^{14}\,\mathrm{cm}^{-3}$. At such high electron densities, the discharge produces a condition close to local thermodynamic equilibrium and results in very high gas temperatures, above 3000 °C.[28] In comparison, the gas temperature in the APPJ is maintained at ~100 °C with the water cooling of the ground electrode, thus thermal damage to the materials treated can be easily avoided.

Finally, we will briefly mention some fundamental issues that are important for the practical use of the α-mode capacitive discharge at atmospheric pressure, yet beyond the scope of this study. For example, the discharge property is sensitive to the gas composition as shown in Fig. 7. Since the use of various reactive gases is critical for materials applications, it is important to include the atomic physics and gas phase chemistry into the overall discharge analysis. This may help to overcome the current restriction on the gas composition for stable α-mode discharges at atmospheric pressure. It is also important to understand the mechanism for the α-mode failure and the scaling of the critical input power of arcing for various discharge parameters, as the reaction rates generally increase with input power. In addition, it is of interest to find out whether it is possible to control the ion energy in the sheath at atmospheric pressure, in order to provide directional etching and ion-assisted chemical reactions on the materials surface.

V. CONCLUSIONS

The principal conclusion of this study is that the discharge produced in the APPJ is essentially an α-mode capacitive discharge at atmospheric pressure. This is based on the experimental measurements that show a close similarities to rf α-mode capacitive discharges for gas lasers. A dimensional analysis was then made to explain the observed discharge phenomena such as spatial structure of the discharge and functional dependence of $I-V$ characteristics using the existing theories of the rf capacitive discharge. In addition, a rough estimate is made for a plasma density of $3 \times 10^{11}\,\mathrm{cm}^{-3}$ and an electron temperature (T_e) of ~2 eV, along with the measured gas temperature of ~120 °C. These plasma parameters indicate that the APPJ shows promise for various materials applications as it can produce substantial amount of reactive species and avoid thermal damage.

ACKNOWLEDGMENTS

The authors would like to thank Dr. C. P. Munson of Los Alamos National Laboratory and Professor C. S. Chang at New York University for their helpful discussion. This work was supported in part by funds provided by the University of California, and in part by funds provided by the U.S. Department of Energy, Environmental Management Sciences Program, and Chemical and Biological Nonproliferation Program (DoE NN-20 CBNP).

[1] *Plasma Etching: An Introduction*, edited by D. M. Manos and D. L. Flamm (Academic, New York, 1989).
[2] M. A. Lieberman and A. J. Lichtenberg, *Plasma Discharges and Materials Processing* (Wiley, New York, 1994).
[3] A. Schütze, J. Y. Jeong, S. E. Babayan, J. Park, G. S. Selwyn, and R. F. Hicks, IEEE Trans. Plasma Sci. **26**, 1685 (1998).
[4] J. Y. Jeong, S. E. Babayan, V. J. Tu, J. Park, R. F. Hicks, and G. S. Selwyn, Plasma Sources Sci. Technol. **7**, 282 (1998).
[5] S. E. Babayan, J. Y. Jeong, V. J. Tu, J. Park, G. S. Selwyn, and R. F. Hicks, Plasma Sources Sci. Technol. **7**, 286 (1998).
[6] H. W. Hermann, I. Henins, J. Park, and G. S. Selwyn, Phys. Plasmas **6**, 2284 (1999).
[7] J. Park, I. Henins, H. W. Herrmann, G. S. Selwyn, J. Y. Jeong, R. F. Hicks, D. Shim, and C. S. Chang, Appl. Phys. Lett. **76**, 288 (2000).
[8] H. Koinuma, H. Ohkubo, T. Hashimoto, K. Inomata, T. Shiraishi, A. Miyanaga, and S. Hayashi, Appl. Phys. Lett. **60**, 816 (1992).
[9] J. R. Roth, *Industrial Plasma Engineering: Principles* (Institute of Physics, Bristol, 1995), Vol. 1.
[10] R. H. Stark and K. H. Schoenbach, J. Appl. Phys. **85**, 2075 (1999).
[11] M. Moisan, Z. Zakrzewski, R. Etemadi, and J. C. Rostaing, J. Appl. Phys. **83**, 5691 (1998).
[12] N. A. Yatsenko, Zh. Tekh. Fiz. **51**, 1195 (1981).
[13] D. He and D. R. Hall, IEEE J. Quantum Electron. **20**, 509 (1984).
[14] H. E. Hugel, Proc. SPIE **650**, 2 (1986).
[15] Y. P. Raizer, M. N. Shneider, and N. A. Yatsenko, *Radio-Frequency Capacitive Discharges* (CRC, Boca Raton, FL, 1995).
[16] S. M. Levitskii, Zh. Tekh. Fiz. **27**, 970, 1001 (1957).
[17] V. A. Godyak and A. S. Khanner, IEEE Trans. Plasma Sci. **14**, 112 (1986).
[18] P. Vidaud, S. M. Durrani, and D. R. Hall, J. Phys. D **21**, 57 (1988).
[19] J. H. Miller, R. W. Boese, and L. P. Giver, J. Quant. Spectrosc. Radiat. Transf. **9**, 1507 (1969).
[20] H. D. Babcock and L. Herzberg, Astrophys. J. **108**, 167 (1948).
[21] W. H. J. Childs and R. Mecke, Z. Phys. **68**, 344 (1931).
[22] M. A. Lieberman, IEEE Trans. Plasma Sci. **17**, 338 (1989).
[23] P. P. Vitruk, H. J. Baker, and D. R. Hall, J. Phys. D **25**, 1767 (1992).
[24] *Electrical Breakdown of Gases*, edited by J. M. Meek and J. D. Craggs (Wiley, Chichester, 1978).
[25] R. N. Franklin, *Plasma Phenomena in Gas Discharges* (Oxford University Press, Oxford, 1976).
[26] L. G. H. Huxley and R. W. Crompton, *The Diffusion and Drift of Electrons in Gases* (Wiley, New York, 1974).
[27] L. S. Frost and A. V. Phelps, Phys. Rev. **127**, 1621 (1962).
[28] M. I. Boulos, IEEE Trans. Plasma Sci. **19**, 1153 (1991).

Downloaded 17 Jan 2003 to 128.97.84.125. Redistribution subject to AIP license or copyright, see http://ojps.aip.org/japo/japcr.jsp